Research Article

An Improved Feedforward-Robust Algorithm for Active Vibration Control of Helicopter Maneuver Flight

Yifan Qin [ID], **Yang Lu** [ID], **and Huiyu Yue** [ID]

National Key Laboratory of Rotorcraft Aeromechanics, College of Aerospace Engineering, Nanjing University of Aeronautics and Astronautics, Nanjing 210016, China

Correspondence should be addressed to Yang Lu; njluyang@163.com

To solve the problem of secondary path mutation and external disturbance abrupt changes during helicopter maneuver flight, the previous research proposed a hybrid active vibration control law. To improve the engineering applicability, the original algorithm is ameliorated to the least mean square-input-output-based robust (LMS-IOBR) algorithm. The system model within the target frequency band can be identified through the input-output data to avoid constructing complex state observers. In addition, the output form of the feedback controller is constructed by an autoregressive moving average model with extra input, which is beneficial to improve operational efficiency. Numerical simulations demonstrate that compared with the original algorithm, controller real-time computation can be reduced by 52% with control effects guaranteed at the same time. Furthermore, to verify the effectiveness and adaptability of LMS-IOBR, multi-input multioutput vibration control experiments are carried out on a specially developed simple platform for simulating helicopter maneuver states. Comparative tests in various typical states are performed between the LMS-IOBR and the multichannel least mean square algorithm. Under the complex circumstances of simulating continuous subduction uplift, the peak response of closed-loop system attenuates by 80% and 70%, and the vibration of two points is reduced to 15% and 20%, respectively, within 3 s. The experimental results demonstrate that the proposed LMS-IOBR algorithm shows stronger transient adaptability and robustness against external disturbance excitation and secondary channel mutation in helicopter maneuver flight.

1. Introduction

In helicopter flight, the rotor cyclic loads generated by unsteady airflow and hub torque are transmitted to the fuselage via the rotor control system and the main gearbox, leading to serious harmonic vibration and posing threats to driving safety and comfort. The active control of structural response (ACSR) technology utilises the actuators installed on the fuselage to generate secondary response to minimize the airframe vibration, which has been successfully applied to some helicopters like EH-101, EC225, UH-60M, and S-92 [1–4]. In recent years, piezoelectric stack actuator (PSA) has gained extensive attention in the active vibration control of local structures, such as helicopter tail beam and main gearbox, due to its small mass volume, wide control frequency band, and fast response speed [5, 6].

However, existing ACSR systems are mainly designed for vibration suppression of helicopter steady flight, and active vibration control in maneuver state gains minor attention [1–4]. Firstly, as is displayed in the measured acceleration response of a CH-53G helicopter when performing acceleration and deceleration, the alternating rotor aerodynamic load alters violently and leads to serious vibration during helicopter large overload maneuver [7–9]. On the other hand, the rotor power demand changes drastically, contributing to excitation frequency fluctuations in a short time [9, 10]. When Bell 427 helicopter turns left, the frequency oscillation occurs, and the rotor rotating speed could be reduced by 5% at most [11]. Furthermore, the control performance is restricted by the sudden change of the secondary path [12]. The results of Z-11 helicopter flight tests demonstrate that vertical vibration reduction efficiency varies from 30% to 66% at different flight speeds, but the control system

converged and then diverged several times during maneuver flight [13]. Therefore, for better adaptive performance, it is necessary to find a new method to enhance the robustness of the control law.

Conventional helicopter vibration control laws mainly include the frequency-domain higher harmonic control (HHC) and the time-domain filtered-x least mean square (Fx-LMS) algorithm. Based on linear and quasistatic assumptions, frequency-domain HHC can effectively reduce steady-state harmonic vibration [2, 4]. However, due to the block processing characteristics of the discrete Fourier transform, the control output and sampling of uncontrolled response are unable to be synchronized, which contributes to slow updating speed and poor adaptability in face of rapid changes of disturbance amplitude, frequency, and system parameters [14, 15]. The time-domain Fx-LMS shows good narrowband control effects and signal tracking ability without accurate system model, but the algorithm performance depends heavily on the correlation between reference signal and excitation [16]. In addition, the offline modeling error caused by actual secondary channel mutation will reduce the adaptive ability and even cause the system to diverge [8].

In recent years, some algorithms applicable to uncertain external disturbances and nonlinear systems have been proposed, and metaheuristic learning algorithm is one of the potential effective methods. For uncertain nonlinear systems with specified-time guaranteed behaviours, many event-triggered neural intelligent control methods are proposed [17, 18]. Moreover, for quadrotors concerning external disturbances and parametric uncertainties, several compensation trajectory tracking strategies and quadrotor attitude tracking control strategies are presented [19–22]. To solve the severe external disturbances, a series of robust control schemes based on back-stepping and disturbance estimator are designed [23, 24]. However, there are some difficulties with these algorithms applying to helicopter active vibration suppression. On the one hand, helicopter ACSR methods emphasize disturbance attenuation ability, while metaheuristic learning algorithms are designed for flight control and focus on the command tracking performance. On the other hand, control target of helicopter vibration changes rapidly, and more importance needs to be attached to the tracking accuracy of frequency and phase changes in the algorithm design.

Given the problems such as time-varying excitation and secondary path mutation in helicopter maneuver flight, the authors put forward a filtered least mean square-mixed sensitivity robust controller (LMS-MSRC) based on the reference signal reconstruction in the previous research, driving a PSA to suppress harmonic vibration [25]. Real-time changes of external disturbance are able to be tracked by the reconstructed reference signal, helping to accelerate system convergence. Besides, the H_∞ feedback controller designed by parameter perturbation reduces the sensitivity to secondary path changes, which is conducive to enhance the robustness. Although these advantages are attractive for ACSR in helicopter maneuver flight, the algorithm engineering applicability still needs improvement in practice.

In subsequent tests, it is found that due to the electromechanical coupling phenomenon, actuator boundary condition changes have a negative impact on the PSA dynamic output characteristics. For helicopters equipped with PSAs, changes in flight conditions will lead to secondary channel mutation [26]. Therefore, the state observer is often required to accurately build secondary channel model, and many efforts are in demand for algorithm design. Furthermore, the controller designed with the state-space model requires a large amount of real-time computation, which exerts heavy burden on hardware resources in engineering practice.

For ensuring vibration suppression effects as well as computing efficiency improvement, an improved LMS-IOBR algorithm based on an autoregressive moving average model with extra input (ARMAX) is proposed. The main contributions in this paper are summarized as follows:

(i) Different from the modeling strategy of the existing LMS-MSRC method [25], the past and current values of system inputs and outputs within the target frequency band are needed for LMS-IOBR to obtain a relatively accurate model. The transfer characteristics of the secondary path could be obtained with less computation, which is conducive to reduce the controller design burden

(ii) Compared with the previous work [25] that uses complex state observers to calculate real-time output, the ARMAX model is utilized to construct the output form of the feedback controller, beneficial to improve operational efficiency and reduce real-time hardware calculation

The main contents are arranged as follows: the second chapter introduces the design process of the LMS-IOBR algorithm. In the third chapter, the simplified helicopter finite element model is taken to conduct simulations to compare control effects before and after algorithm improvement. A simple experiment platform for simulating the vibration environment on helicopter maneuver conditions is introduced in the fourth chapter. The fifth section presents a series of multi-input multi-output ACSR experiment results and analyses. Some conclusions are summarized at the last.

2. Improved LMS-IOBR Algorithm Design

To better describe the improved LMS-IOBR, the previous LMS-MSRC algorithm is introduced, and its shortcomings of engineering application during maneuver flight are analyzed. Furthermore, the specific improvement measures of system modeling and feedback controller design are put forward.

2.1. Helicopter ACSR LMS-MSRC Method. At an early stage of research, a hybrid helicopter ACSR scheme was proposed by combining the robust feedback controller with time-domain LMS feedforward controller. The LMS-MSRC control framework is illustrated in Figure 1. $v(n)$ is the rotor harmonic excitation, and $P(z)$ denotes the primary channel. $d(n)$ is the vibration response after $P(z)$, indicating a
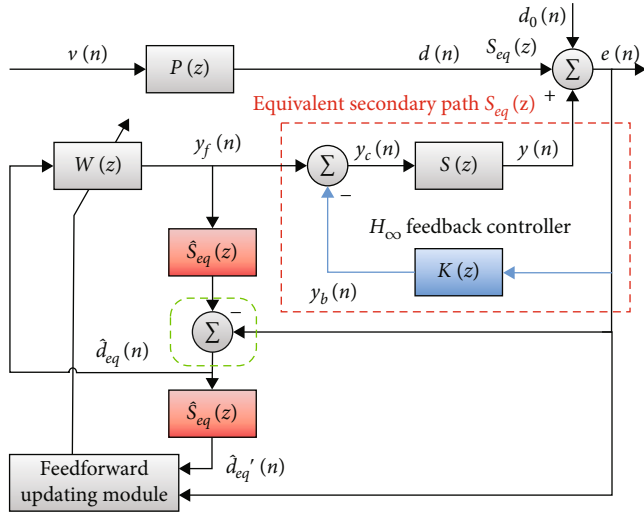
FIGURE 1: Block diagram of the previous LMS-MSRC algorithm for helicopter ACSR. The red box describes the equivalent secondary path, and the green one shows reference signal reconstruction.

multifrequency component at the target point (e.g., the pilot's position). $\mathbf{d}_0(n)$ represents the undetectable disturbance signal. $\widehat{d}_{eq}(n)$ is the reference signal reconstructed in real-time via the error signal $e(n)$. $S(z)$ reveals the actual secondary path, including D/A, driving amplifier, actuator, dynamic characteristics between actuator and error sensor, and so on. $K(z)$ is the H_∞ feedback controller. $S_{eq}(z)$ indicates the equivalent secondary path formed by $S(z)$ and $K(z)$. $\widehat{d}_{eq}'(n)$ is the filtered reference signal after $\widehat{d}_{eq}(n)$ filtered by equivalent secondary path offline estimation $\widehat{S}_{eq}(z)$. $W(z)$ denotes a feedforward FIR filter. $y_f(n)$ and $y_b(n)$ are the output signal of $W(z)$ and $K(z)$ independently.

Hence, the LMS-MSRC algorithm is summed up as follows [25]:

$$
\begin{aligned}
y_f(n) &= W(n) * \widehat{D}_{eq}(n), \\
y_c(n) &= y_f(n) + y_b(n), \\
e(n) &= d(n) + d_0(n) - S(z) * Y_c(n), \\
\widehat{d}_{eq}(n) &= e(n) + \widehat{S}_{eq}(z) * Y_f(n), \\
\widehat{d}_{eq}'(n) &= \widehat{S}_{eq}(z) * \widehat{D}_{eq}(n), \\
W(n+1) &= W(n) + 2\mu e(n)\widehat{D}_{eq}'(n),
\end{aligned}
\tag{1}
$$

where $\widehat{D}_{eq}(n)$, $Y_c(n)$, $Y_f(n)$, and $\widehat{D}_{eq}'(n)$ denote the time series of $\widehat{d}_{eq}(n)$, $y_c(n)$, $y_f(n)$, and $\widehat{d}_{eq}'(n)$ separately. The equivalent secondary path $S_{eq}(z)$ constructed by the feedback controller $K(z)$ is expressed as [25]:

$$
S_{eq}(z) = \frac{S(z)}{1 + S(z)K(z)}.
\tag{2}
$$

From formulas (1) and (2), it can be seen that in view of the secondary path mutation during helicopter maneuver

flight, LMS-MSRC effectively increases the damping of equivalent secondary channel $S_{eq}(z)$ and reduces the sensitivity to $S(z)$ changes, which is helpful to enhance the system stability. In addition, the influence of $y_f(k)$ on error signal $e(n)$ is counteracted, and the reconstructed signal $\widehat{d}_{eq}(n)$ effectively reflects real-time changes of external excitation, thus speeding up the convergence.

2.2. Improved LMS-IOBR Algorithm. According to the reference [26], secondary path mutation will take place when PSAs are used to suppress helicopter vibration in maneuver flight, which means that when designing feedback controllers, complex state observers are often needed to obtain precise secondary channel model, resulting in a large amount of design work. Furthermore, the heavy real-time computation burden shows adverse effects on engineering application. In order to simplify design process and improve operation efficiency, an improved LMS-IOBR algorithm is proposed to accomplish secondary path modeling by ARMAX and feedback controller design.

2.2.1. Secondary Path Modeling Based on ARMAX. The controller is designed for single-input single-output ACSR system for convenience. As is shown in Figure 2, assuming that the system dynamics model is an ARMAX structure of "controlled object+measurement noise", the discrete-time secondary channel model can be expressed as [27]:

$$
A(z)y(n) = B(z)u(n) + C(z)\zeta(n),
\tag{3}
$$

where n is the discrete sampling time. $u(n)$ and $y(n)$ represent the input voltage and vibration response separately. $\zeta(n)$ is the measurement white noise with the assumption that it is smooth and bounded. And

$$
\begin{aligned}
A(z) &= 1 + a_1 z^{-1} + a_2 z^{-2} + \cdots a_{n_a} z^{-n_a}, \\
B(z) &= b_1 z^{-1} + b_2 z^{-2} + \cdots b_{n_b} z^{-n_b}, \\
C(z) &= c_1 z^{-1} + c_2 z^{-2} + \cdots c_{n_c} z^{-n_c},
\end{aligned}
\tag{4}
$$

where n_a, n_b, and n_c are delay operators z^{-1} order of polynomials $A(z)$, $B(z)$, and $C(z)$, respectively. In practice, through the current and past value of the input signal and output response data, the nominal model and noise model of secondary path can be identified simultaneously so as to obtain more accurate parameter estimation.

2.2.2. Robust Controller Design Using Input-Output Identification Model. Considering the vibration suppression characteristics in helicopter maneuver flight, the controller design of secondary path perturbations is transformed into the robust performance design problem of uncertain parameter systems. For the secondary channel identified using the input-output data, the robust stabilization problem is solved with an appropriate performance weighting function so that a suitable robust controller is obtained, increasing system damping and reducing the sensitivity to secondary path changes at the same time.
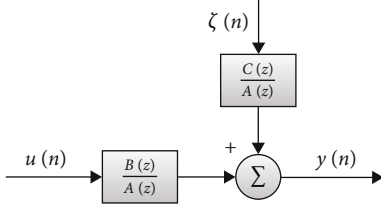
FIGURE 2: Block diagram of secondary path modeling based on ARMAX.

The scheme of the feedback controller design is displayed in Figure 3. The actual secondary channel $S(z)$ based on multiplicative uncertainty consists of a nominal model and a perturbation part. $\Delta S_t(z)$ represents the dynamic parameter perturbation caused by helicopter maneuver action. $B(z)/A(z)$ is the nominal secondary path when $\Delta S_t(z) = 0$, obtained by model identification with input-output data. $d(n) + d_0(n)$, $y_b(n)$, and $e(n)$ are the external disturbance, control, and error signal, respectively.

Assumption 1. The multiplicative uncertainty in secondary path $S(z)$ shows relative errors between the actual dynamics and the nominal model. The parameter perturbation $\Delta S_t(z)$ is uncertain but usually is norm-bounded so that

$$\bar{\sigma}[\Delta S_t(z)] \le \delta(j\omega) \tag{5}$$

where δ can be set to a known scalar function for all frequencies ω.

Remark 2. Note that although the actual parameter perturbation $\Delta S_t(z)$ is unknown, the controller design is based on the upper limit of fluctuation range $\delta(j\omega)$. Therefore, the controller is designed to meet the system robustness requirements.

The transfer function between $d(n) + d_0(n)$ and $y_b(n)$ is defined as the output sensitivity function $H_{ed}(z)$, and that between $d(n) + d_0(n)$ and $e(n)$ is set to input sensitivity function $H_{ud}(z)$. To improve operation efficiency in engineering application, the output form of the feedback controller is designed with the ARMAX model. $H_{ed}(z)$ and $H_{ud}(z)$ are

$$H_{ed}(z) = \frac{A(z)T(z)}{A(z)T(z) + B(z)R(z)},$$

$$H_{ud}(z) = -\frac{A(z)R(z)}{A(z)T(z) + B(z)R(z)}. \tag{6}$$

To ensure control system robustness under secondary channel mutation, it is necessary to confirm output response changes caused by $\Delta S_t(z)$ to satisfy certain performance criteria. According to reference [28], the

following requirements need meeting:

$$\|\Delta S_t(z) \times H_{ed}(z)\|_\infty = \left\|\Delta S_t(z) \times \frac{A(z)T(z)}{A(z)T(z) + B(z)R(z)}\right\|_\infty \le 1. \tag{7}$$

Therefore, to achieve disturbance suppression target in the sense of $\infty-$norm, equation (7) is transformed into a robust stabilization problem, which is solved to gain an appropriate H_∞ feedback controller $R(z)/T(z)$.

Considering the frequency characteristics of excitation and the system complexity reduction, the disturbance suppressing performance should be focused on the target frequency band by designing a reasonable performance weighting function $W_1(z)$. Large amplitude is required at the excitation frequencies to suppress response. For the sake of simplifying complexity and avoiding system natural frequencies, $W_1(z)$ is therefore designed as a narrow band pass filter with excitation frequencies, which is shown in

$$W_1(s) = \lambda \prod_{i=1}^{n} \frac{f_{wi}^2}{s^2 + 2f_{wi}\sigma_i s + f_{wi}^2}, \tag{8}$$

where λ and σ_i indicate the adjustment coefficient and system damping ratio, respectively. f_{wi} is set to disturbance frequencies. As a result, the robust performance objective is adjusted from equation (7) to

$$\left\| W_1(z) \times \frac{A(z)T(z)}{A(z)T(z) + B(z)R(z)} \right\|_\infty \le \frac{1}{\|\Delta S_t(z)\|_\infty}. \tag{9}$$

With MATLAB robust control toolbox and several simulation attempts, proper $W_1(z)$ parameters can be obtained, and a stable robust controller $K(z)$ is designed as a z-domain controller via time-frequency conversion.

Similarly, in order to limit the controller input energy in practice, robust stabilization can be designed for the input sensitivity function $H_{ud}(z)$. Therefore, the objectives of disturbance attenuation and energy reduction can be taken into account simultaneously via mixed sensitivity controller design. Accordingly, the robust stabilization problem that needs solving becomes:

$$\min \left\| \begin{array}{c} W_1(z) \times H_{ed}(z) \\ W_2(z) \times H_{ud}(z) \end{array} \right\|_\infty = \left\| \begin{array}{c} W_1(z) \times \dfrac{A(z)T(z)}{A(z)T(z) + B(z)R(z)} \\ W_2(z) \times \dfrac{A(z)R(z)}{A(z)T(z) + B(z)R(z)} \end{array} \right\|_\infty, \tag{10}$$

where $W_2(z)$ is a high-pass filter, usually taken as constant 1.

3. Numerical Simulations

To verify the effectiveness of the proposed LMS-IOBR, a simplified helicopter finite element model is used to carry out single-input single-output ACSR simulation during maneuver flight. Offline system identification is performed
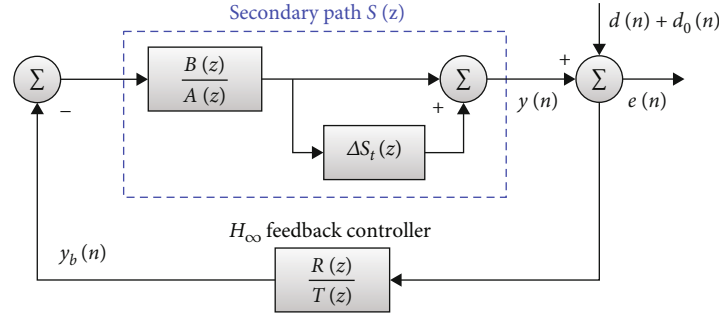
FIGURE 3: H_∞ feedback controller design by $S(z)$ based on multiplicative uncertainty.

based on the ARMAX model to complete the feedback controller design. LMS-MSRC and multichannel LMS simulations are carried out simultaneously for comparison [12, 21]. As a result, the control effects of LMS-IOBR are confirmed in the case of complex external disturbance and secondary path mutation in helicopter maneuver.

3.1. Simplified Helicopter Finite Element Model. In some cases, the helicopter fuselage can be simplified as a slender elastic beam model for vibration response analysis [29]. Figure 4(a) displays a free-free finite element beam model established as the simplified helicopter fuselage in the previous research. The detailed structural parameters are given in Table 1.

To verify the secondary path mutation in maneuver flight, it is necessary to further establish the dynamics model of the airframe installed with a PSA. As is exhibited in Figure 4(b), external excitation is applied at the 94th node to simulate rotor aerodynamic loads. Node 41 stands for the driver's position, where the vibration response measured is regarded as an evaluation target for the overall validity of the ACSR system. The PSA is installed at the 109th node. The vibration response analysis of the helicopter electromechanical coupling beam model built by COMSOL is carried out so that the transfer function between PSA input voltage and target position response is obtained. With the application of the vertical static force at node 3, the PSA boundary conditions are altered so that the new transfer function of the simulated helicopter maneuver flight can be obtained.

Considering the actual demands for vibration attenuation and control system scale, a series of ACSR simulations based on the first two harmonic frequency components (19.5 Hz + 39 Hz) are carried out [30]. The response amplitude of 39 Hz is about 30% of 19.5 Hz by regulating excitation magnitude. Gaussian white noise is added to the multifrequency disturbance signal.

3.2. Secondary Path Identification. It is necessary to obtain the offline model of the secondary path in advance for designing the control law. Compared with the state-space model, the secondary path composed of the ARMAX model can be set to a specific modeling order so that some higher-order modes are ignored. As a result, dynamic characteristics of the system are described more accurately within the target frequency band.

The identification object is the model between the PSA input voltage installed at the 109th node and the vibration response measured at node 41. The sampling rate in the simulation is set to 1000 Hz. The vibration response is obtained by introducing 15~45 Hz white noise, and the secondary path is identified by the ARMAX method. After complexity estimation, the order of polynomial $A(z)$ and $B(z)$ is adjusted to $n_a = 6$ and $n_b = 4$.

Remark 3. Note that the values of n_a and n_b can be determined as the following steps. n_a can be initially determined by input signal frequency band range in system identification. The number of modes covered by the input frequency band determines the value of n_a, which can initially be taken as twice the mode number. Then, after repeated attempts, the order of n_b is adjusted by evaluating the system identification effects.

The accuracy of system identification can be verified by modeling residual $\delta(n)$, which is defined as

$$\delta(n) = y(n) - \theta^T(n)\varphi(n), \tag{11}$$

where

$$\theta^T(n) = [a_1(n), \cdots, a_{n_a}(n), b_1(n), \cdots, b_{n_b}(n)], \tag{12}$$

$$\varphi^T(n) = [-y(n-1), \cdots, -y(n-n_a), u(n-1), \cdots, u(n-n_b)]. \tag{13}$$

The estimated residual and predicted error for the system identification process are demonstrated in Figure 5. The input-output data of the first 4 s is used for model identification. Based on the identification model at the end of 4 s, the output in the following 6 s is predicted from the input data and compared with the desired vibration. The identification results illustrate that the modeling prediction error is only 7.1% in contrast with the desired output, proving that the input-output characteristics of the system are relatively accurately described based on the ARMAX model.

3.3. Computational Complexity Analysis. To highlight the advantages of low complexity for LMS-IOBR, vibration control simulations of LMS-IOBR, multichannel LMS, and LMS-MSRC algorithm are compared. The initial parameter
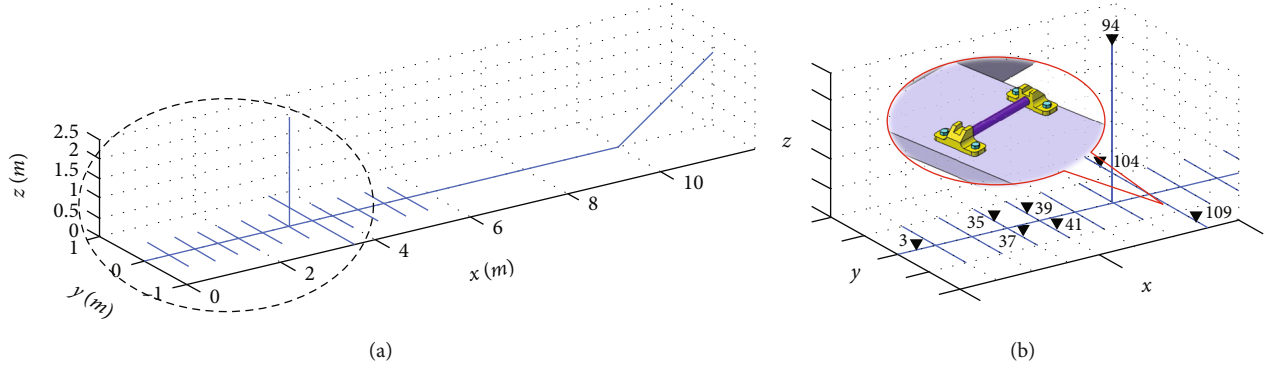
(a)

(b)

FIGURE 4: Simplified finite element model of the helicopter airframe. (a) The whole fuselage. (b) Enlargement of the front airframe.

TABLE 1: Parameters of the beam structure.

Parameters	Data
Mass (kg)	6.0×10^3
Density (kg/m³)	7.8×10^3
Modulus of elasticity (GPa)	2.1×10^2
Poisson's ratio	0.3
First natural frequency (Hz)	8.2, 11.2, 16.7, 26.9, 33.2, 50.4, 56.9
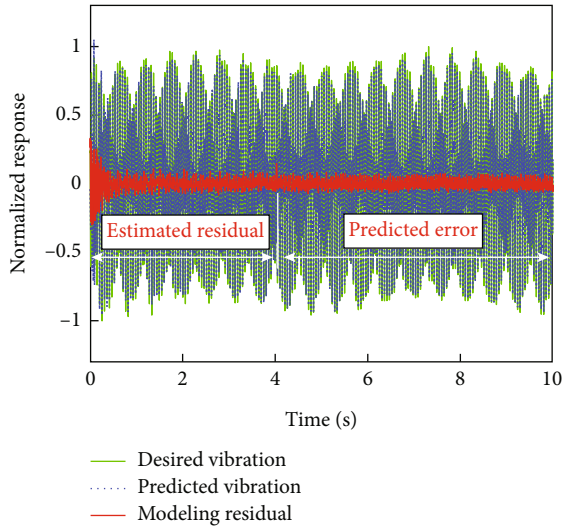
FIGURE 5: Estimated residual and predicted error in system identification.

settings are as follows to ensure the consistency: the sampling rate is set to 1000 Hz. The filter length L is set to 32, and the initial value of the filter coefficient is 0. After several attempts to obtain maximum convergence factors, the convergence factors of multichannel LMS are $\mu_{19.5\,Hz} = 8 \times 10^{-4}$ and $\mu_{39\,Hz} = 2 \times 10^{-3}$. In addition, the value of the LMS-MSRC and LMS-IOBR is $\mu = 5 \times 10^{-2}$. In this way, it is ensured that all three control algorithms can show their optimal performance. The adjustment coefficients, external disturbance frequencies, and system damping

ratio are designed as follows: $\lambda = 0.4$, $f_{wi} = 2\pi \times [19.5, 39]$, and $\sigma_i = [0.06, 0.025]$.

The feedback controller in LMS-MSRC is designed in the form of the state-space model, of which the state vector length is $m_s = 12$. The order of the feedback controller designed by the input-output identification model in LMS-IOBR is $n_T = 7$ and $n_R = 6$. It is apparent that, compared with LMS-MSRC, the feedback controller design in LMS-IOBR is simpler.

The computational complexity of the three algorithms is illustrated in Table 2. M and N represent the modeling FIR filter length of the equivalent secondary path $\widehat{S}_{eq}(z)$ and actual secondary channel $\widehat{S}(z)$, respectively. In subsequent simulations, $M = N = L = 32$. Substituting specific values into calculation, it is found that the complexity of multichannel LMS, LMS-MSRC, and LMS-IOBR is 513, 596, and 284, respectively, in each update. Compared with LMS-MSRC using the state-space model, the complexity of LMS-IOBR is reduced by 52%, resulting in a great reduction of real-time computational burden.

3.4. Numerical Results and Analysis. To verify the robustness and adaptability of LMS-IOBR applied to helicopter ACSR in maneuver flight, it is compared with multichannel LMS and LMS-MSRC in vibration control simulations.

Remark 4. Note that to ensure fairness in comparison of the simulation results, the control system parameter consistency is set in the following aspects: (1) initial parameter settings of control system, (2) convergence factors and optimal control performance, and (3) external disturbance excitation and secondary channel mutation. Through the above three measures, it is ensured that the differences in control effects are caused by the performance of the three algorithms. In all simulation examples, the controller parameters of each algorithm remain unchanged.

3.4.1. Secondary Path Mutation and Additional Transient Perturbation. The control started at 10 s. To realize secondary channel changes and transient aerodynamic interference caused by a gust in maneuver flight, the control channel is replaced by a new transfer function at 30 s, and extra perturbation is applied at 50 s. The comparison of the three algorithms is illustrated in Figure 6.

TABLE 2: Computational complexity.

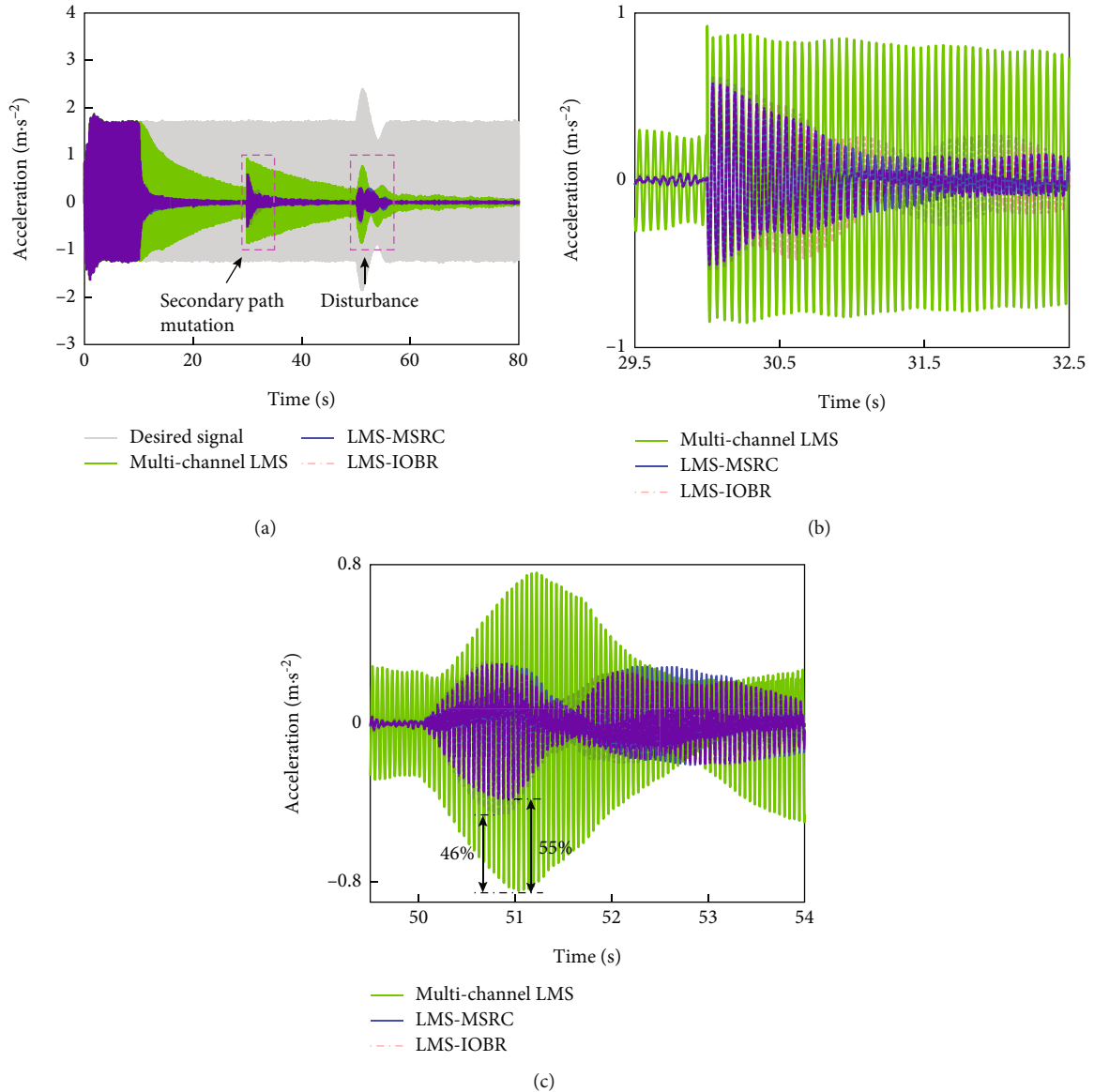|	Multiplications	Additions	In Total
Multichannel LMS	$6L + 2N$	$6L + 2N + 1$	$12L + 4N + 1$
LMS-MSRC	$2L + 2M + (m + 1)^2$	$2L + 2M + 2 + (m_s + 1)^2$	$4L + 4M + 2 + 2(m_s + 1)^2$
LMS-IOBR	$2L + 2M + (n_T + n_R)$	$2L + 2M + 2 + (n_T + n_R)$	$4L + 4M + 2 + 2(n_T + n_R)$

(a)

(b)

(c)

FIGURE 6: Comparison of acceleration response with 3 different helicopter ACSR methods. (a) Acceleration response. (b) Control process at secondary path mutation (29.5-32.5 s). (c) Control process at additional perturbation (49.5-54 s).

As we can see from Figure 6(a), acceleration response decreases to 16% after multichannel LMS controls for 20 s, while the two hybrid methods converge rapidly so that the multifrequency vibration components are completely suppressed after 7 s. Figures 6(b) and 6(c) separately display the vibration control process when secondary channel is abruptly changed and additional perturbation is applied. It

is of the slowest convergence speed for multichannel LMS among all 3 methods to adjust to secondary path changes. Moreover, for lack of necessary reference information, multichannel LMS exhibits poor adaptive performance for extra disturbance, but response overshoot of LMS-MSRC and LMS-IOBR is reduced by 55% and 46%, respectively. In comparison with LMS-MSRC, although the controller
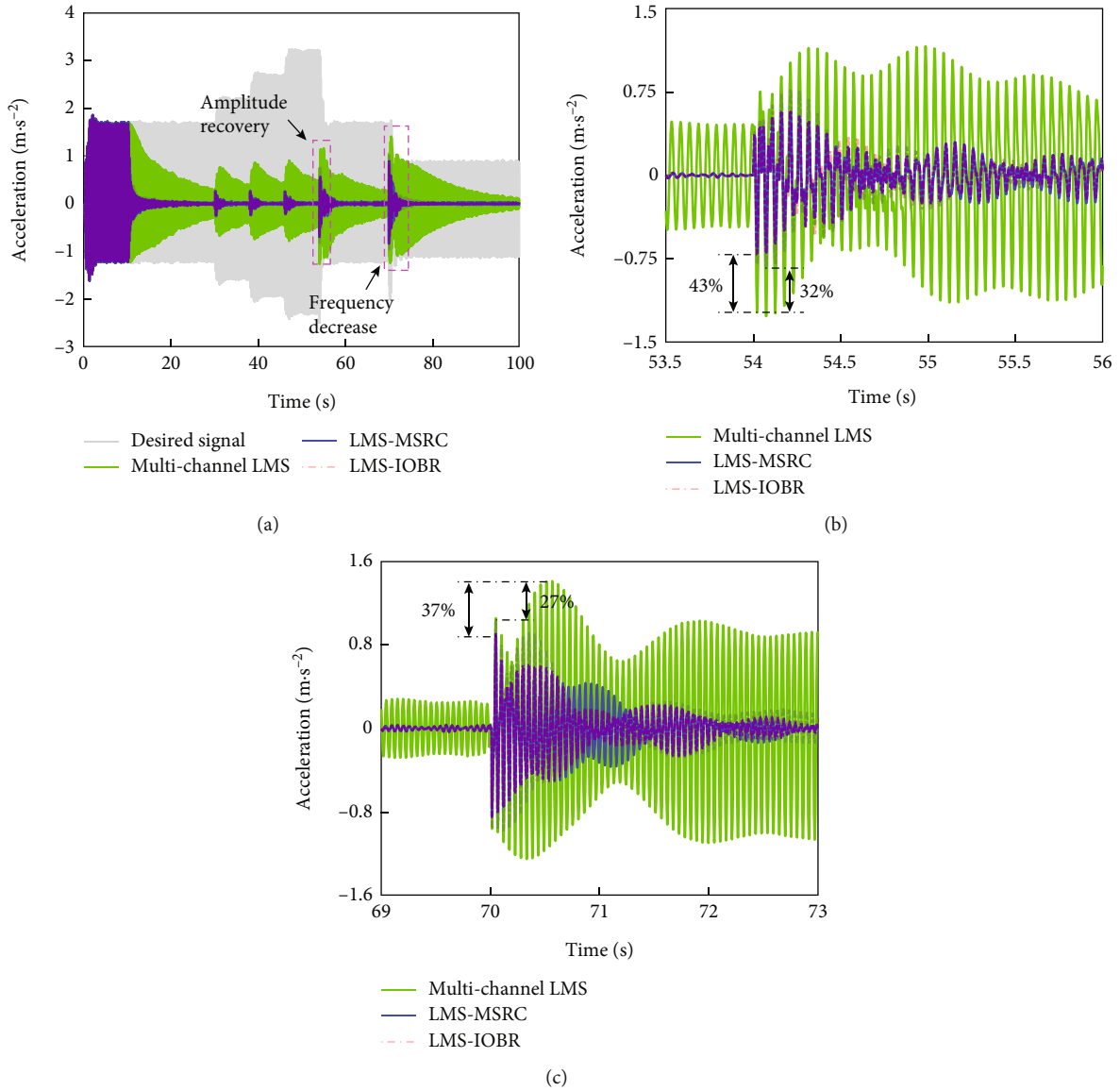
(a)

(b)

(c)

FIGURE 7: Comparison of acceleration response with 3 different helicopter ACSR methods. (a) Acceleration response at control point. (b) Control process at amplitude recovery (53.5-56 s). (c) Control process at frequency reduction (69-73 s).

designed using the ARMAX model in LMS-IOBR has more vibration response oscillations, it shows strong inhibition performance against dynamic parameter changes and uncertain transient disturbance, which helps to enhance system robustness and adaptability in maneuver flight.

3.4.2. Harmonic Force with Time-Varying Magnitude and Frequency. Taking the helicopter accelerating forward flight condition for example, harmonic force amplitude increases 30% every 8 s from 30 s on and returns to original at 54 s. Disturbance frequency is reduced by 5% (18.5 Hz + 37 Hz) at 70 s to simulate the decrease of engine output during maneuver flight. The control started at 10 s, and the vibration control process is illustrated in Figure 7.

As is shown in Figure 7(a), for external vibration with continuously changing amplitude and frequency, the convergence speed of multichannel LMS is slow. In contrast, the hybrid controller with LMS-MSRC exhibits better convergence. It can be found from Figures 7(b) and 7(c) that global vibration attenuation reaches 90% within 2 s at amplitude recovery and frequency decrease, and response overshoot of the closed-loop system drops 43% and 37%, respectively. Compared to this, although the overshoot suppression effects of LMS-IOBR are weakened, the reconstructed reference signal could effectively track vibration response changes, making it beneficial to ensure system stability and accelerate convergence speed.

It is not hard to draw the conclusions with the above simulation results: compared with multichannel LMS, two
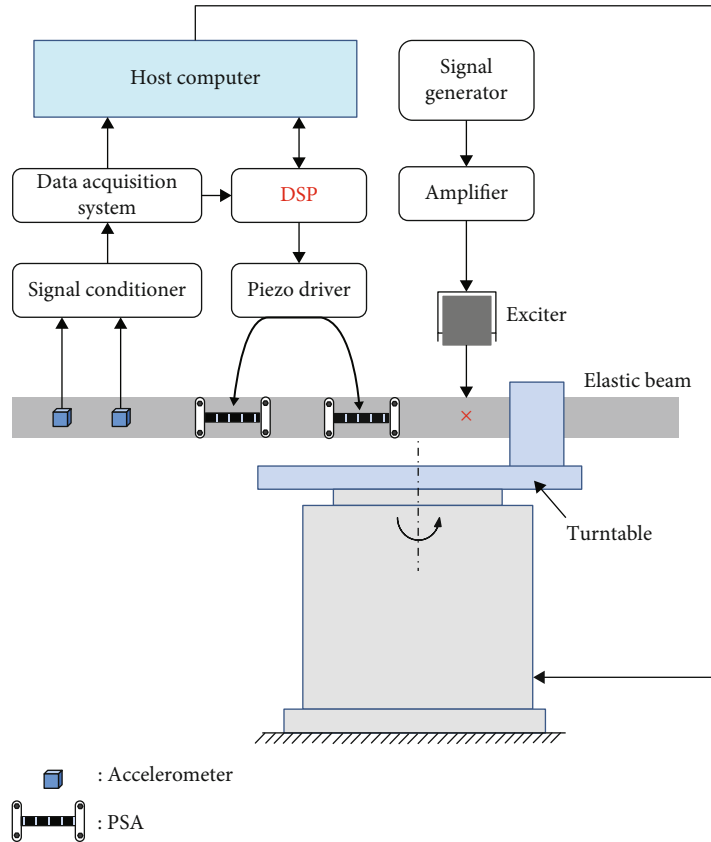
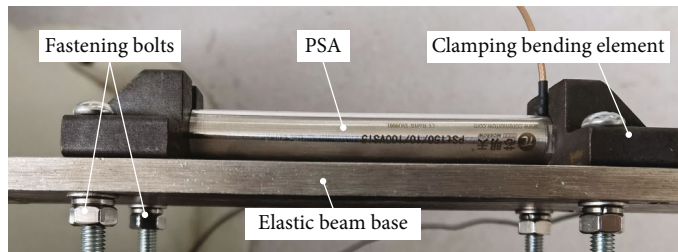FIGURE 8: Block diagram of the elastic beam rotary ACSR test system.

FIGURE 9: Actuation system mounted on the elastic beam.

TABLE 3: Parameters of the piezoelectric stack.

Parameters	Data
Peak-to-peak displacement (μm)	100
Axial stiffness (N/m)	2.0×107
Blocked force (N)	3.5×103
First axial natural frequency (kHz)	10
Diameter × length (mm)	15×100
Input range (V)	0~150

TABLE 4: Parameters of the beam structure.

Parameters	Data
Length × width × height (mm)	$1200 \times 8 \times 80$
First three natural frequency (Hz)	6.9, 43.5, 79.0
Control points (mm)	100, 180
Actuator location (mm)	300, 530
Exciter location (mm)	740

hybrid algorithms perform faster convergence as well as better robustness, showing great self-adaptability to complicated conditions in helicopter maneuver flight. There is no need for LMS-IOBR designed based on input-output identi-

fication model to obtain accurate state model. In contrast with LMS-MSRC, real-time calculation of the hybrid controller is reduced, and vibration suppression effects can be guaranteed at the same time, which is more conducive to engineering implementation.
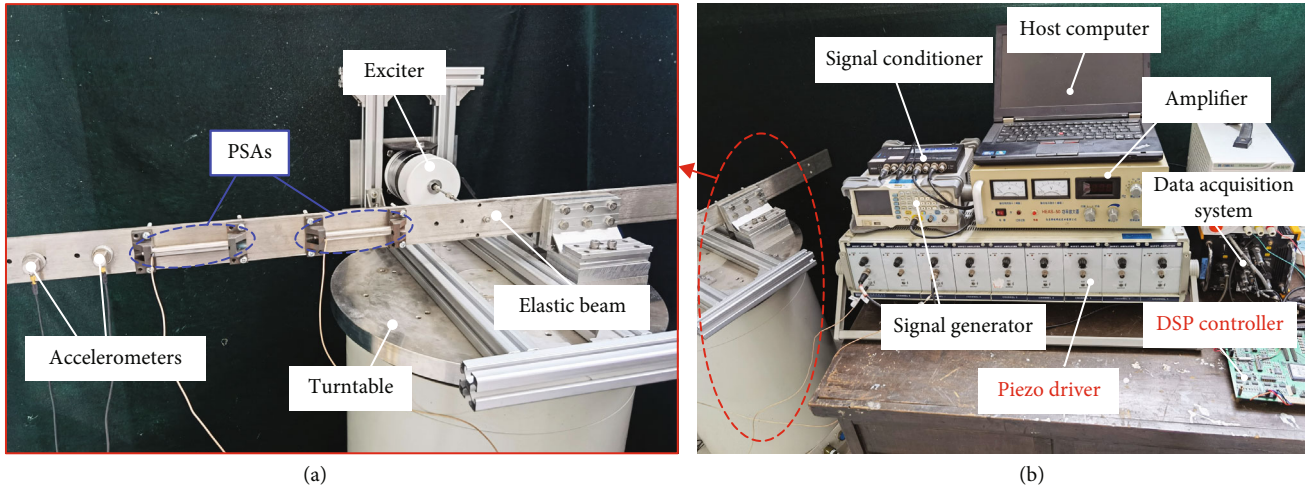
FIGURE 10: Physical diagram of the elastic beam rotary ACSR experiment system. (a) Elastic beam rotary test bench. (b) Measurement and control system.

4. Elastic Beam Rotary ASCR Experiments

In order to validate the proposed method under complex working conditions, multi-input multi-output harmonic experiments are conducted with the developed elastic beam rotary ASCR test system. The platform drives the elastic beam to reciprocate via a single-axis turntable, causing continuous changes in the PSA boundary conditions and system parameters to simulate the vibration environment in helicopter maneuver stage.

The elastic beam rotary ACSR test system is established in Figure 8. The elastic beam fixed to the single-axis turntable represents the floor structure of helicopter front airframe. The signal generator (1000Z, DG) outputs multifrequency signal, which drives the electromagnetic exciter (HEA-50, Sinocera) mounted on the turntable to generate dynamic loads via the power amplifier. Two points on the front of the elastic beam (simulating the drivers' seats) are chosen as control positions, where measured vibration enters the data acquisition system (DH5902, Donghua) after low-pass filtering by a signal conditioner (CM3504, Centuryl). The single-axis turntable (C10T45A, Suline) is able to rotate around the central axis, simulating the real-time changes of the fuselage pitch angle during maneuver flight.

As is illustrated in Figure 9, the actuation composed of PSAs is set to the elastic beam by rigid clamping bending elements and fastening bolts. PSAs convert axial force into local bending moments with this coupling mechanism to suppress structural bending vibration. Parameters of the piezoelectric stack (PJ 100VS15) are shown in Table 3. The PSA output force is up to 3500 N under low-voltage driving conditions, with higher mechanical output efficiency and sufficient power.

The DSP (C6747, TI) calculates real-time signal according to the active control law, which drives the PSAs to generate the desired torque so as to cancel the response caused by external excitation. Table 4 reveals the structural param-
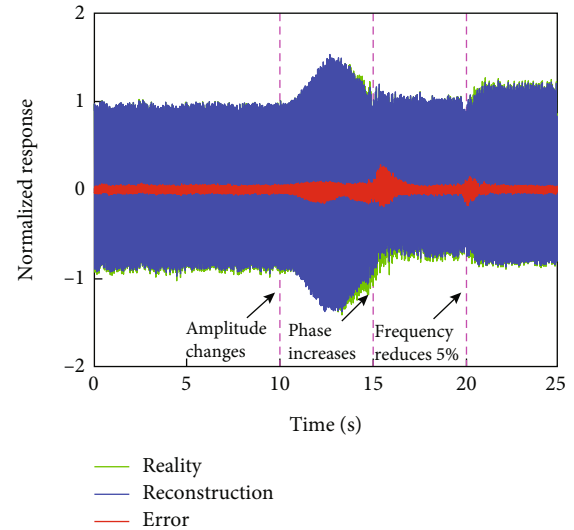

FIGURE 11: Comparison between the reality and construction signal.

eters of the elastic beam, and a physical diagram of ACSR experiment system is displayed in Figure 10.

5. Results and Analysis of ACSR Experiments

Comparative ACSR experiments have been conducted between multichannel LMS and the improved hybrid algorithm to verify the effectiveness of LMS-IOBR. The test steps are as follows: firstly, the accuracy of reference signal reconstruction is verified. In addition, the adaptive performance of the hybrid controller to the secondary channel mutation is validated and analyzed. Then, the control tests are carried out for time-varying amplitude, phase, and frequency of rotor loads during maneuver flight. At last, taking all the above factors into consideration and driving the elastic beam to rotate continuously, the transient disturbance suppression
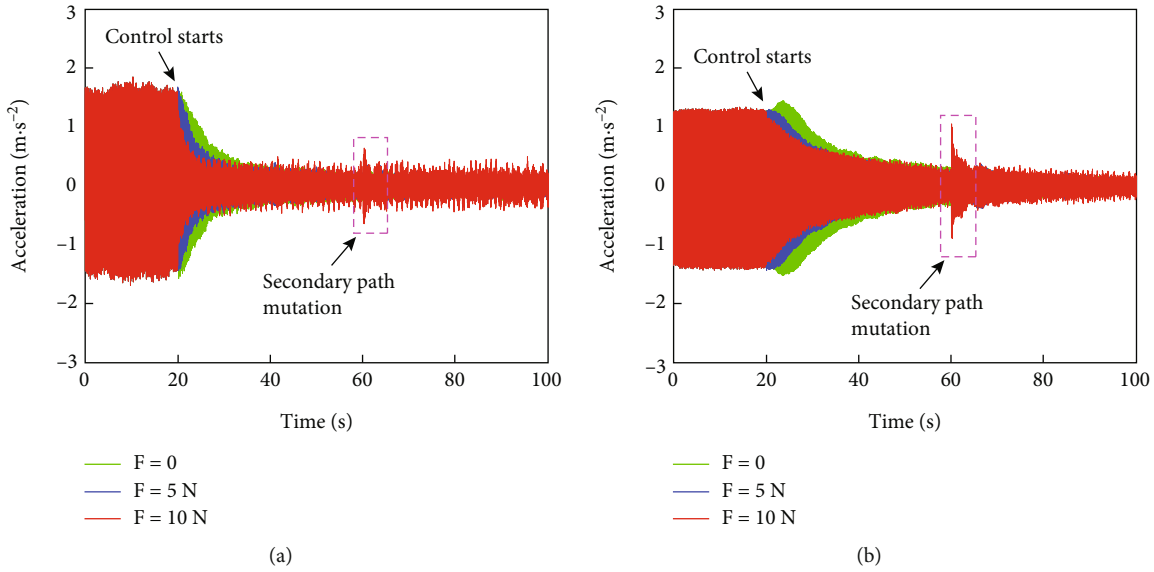
Figure 12: Acceleration response with multichannel LMS. (a) 1# point. (b) 2# point.

and convergence performance are verified under the complex condition of simulating continuous subduction uplift.

After several attempts, the convergence step of multichannel LMS is set to $\mu_{19.5\,Hz} = 2 \times 10^{-3}$ and $\mu_{39\,Hz} = 6.5 \times 10^{-3}$ while that of LMS-IOBR is $\mu = 3.5 \times 10^{-2}$. The sampling rate is 1000 Hz. The filter order is set to 32 and the initial value is 0. The adjustment coefficient λ, external disturbance frequency f_{wi}, and system damping ratio σ_i are designed as follows: $\lambda = 0.28$, $f_{wi} = 2\pi \times [19.5, 39]$, and $\sigma_i = [0.095, 0.04]$.

5.1. Reference Signal Reconstruction Test.

To prove the accuracy of the reconstructed reference signal, the uncontrolled response at 1# control point is chosen as the reconstruction signal. The reality and reconstruction signal are compared in Figure 11. At 10 s, 15 s, and 20s, the amplitude, phase, and frequency of the excitation signal change, respectively, and all response signals are normalized by the peak value before 10 s. It can be seen that the reconstruction signal is in good consistency with the reality, and the overall error is less than 6.1%. Although reconstructed error increases after 15 s, it does not show a divergent trend, which reveals that the reconstructed signal performs good tracking ability to the reality signal changes. From the subsequent tests, such reconstruction error is acceptable, and the LMS-IOBR hybrid controller works well.

5.2. Secondary Path Mutation Experiments.

The cantilever beam on the turntable remains stationary before control. To simulate the system parameter changes in helicopter maneuver flight, different lateral static forces F are applied at the top of the beam so as to accomplish different changes in the secondary channel. The control starts at 20 s. The static force is unloaded at near 60 s, and secondary paths return to original value.

The vibration control process is illustrated in Figures 12 and 13. LMS-IOBR shows faster convergence than multi-

channel LMS with the same secondary channels. When the static force $F = 0$, the acceleration response of 1# and 2# points attenuate 20% and 30%, respectively, with application of multichannel LMS for 14 s and 25 s. However, LMS-IOBR converges rapidly, and the vibration response of the two controlled points achieves same vibration suppression after 5 s. Multichannel LMS shows more sensitivity to secondary path changes, and the system convergence changes significantly. Both methods could adapt to secondary path mutation, but the convergence of multichannel LMS is slower, while LMS-IOBR performs stronger stability and robustness by contrast.

Figures 14 and 15 display the acceleration response with multichannel LMS and LMS-IOBR at secondary path mutation independently. It reveals that the greater the static force F exerted on the cantilever, the more secondary channel changes after force is unloaded. When $F = 10$ N, transient vibration response with multichannel LMS reaches 0.6 m/s^2 and 0.48 m/s^2. In contrast, the response overshoot of LMS-IOBR is only 0.4 m/s^2 and 0.48 m/s^2, which is reduced by 33% and 52%, respectively.

The secondary path has a great impact on the adaptability and stability of the control system, and it is of significance to analyse system frequency response function before and after dynamic parameter changes. Figures 16(a) and 16(b) show that, before and after unloading of static force $F = 10$ N, actual secondary path $G_{11}(\omega)$ and equivalent secondary channel $Geq_{11}(\omega)$ from 1# PSA to 1# point change a lot. The value of $G_{11}(\omega)$ before mutation is $G_{11}(\omega_1) = -2.42 \times 10^{-2} + 0.402 \times 10^{-2} i (\text{m} \cdot \text{s}^{-2}/\text{V})$, and it becomes $\hat{G}_{11}(\omega_1) = -4.21 \times 10^{-2} + 0.431 \times 10^{-2} i (\text{m} \cdot \text{s}^{-2}/\text{V})$ after mutation. Re $(G_{11}(\omega_1))$ and Im $(G_{11}(\omega_1))$ represent the real and imaginary part of $G_{11}(\omega_1)$, respectively. $G_{11}(\omega)$ and $Geq_{11}(\omega)$ before and after system parameter mutation are illustrated in Table 5.

It can be seen that the actual secondary channel $G_{11}(\omega)$ changes severely within 2 s after 60 s. Phase error is
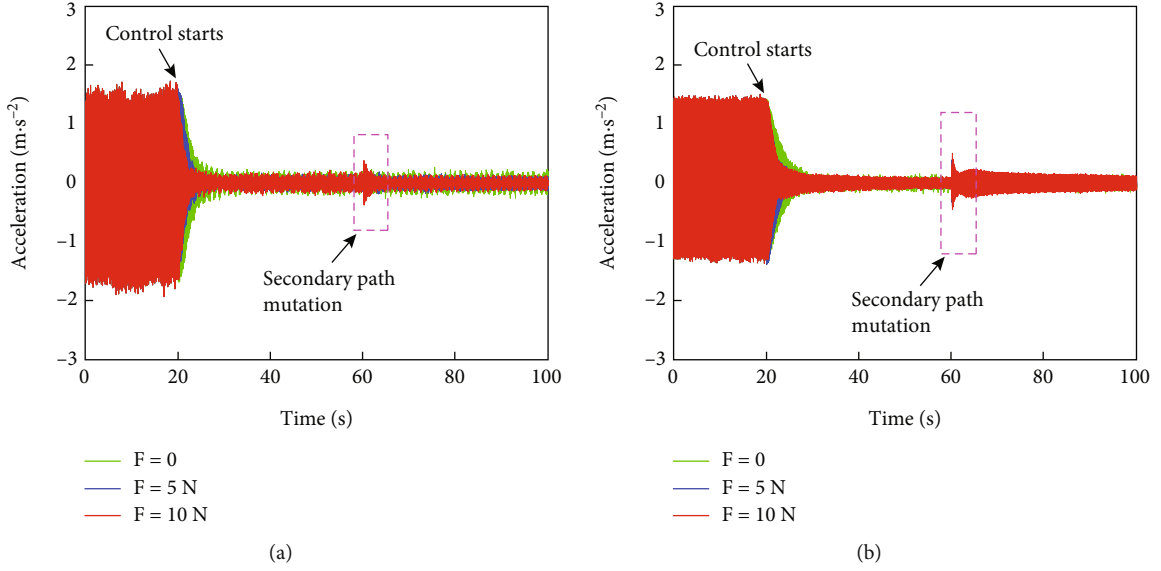
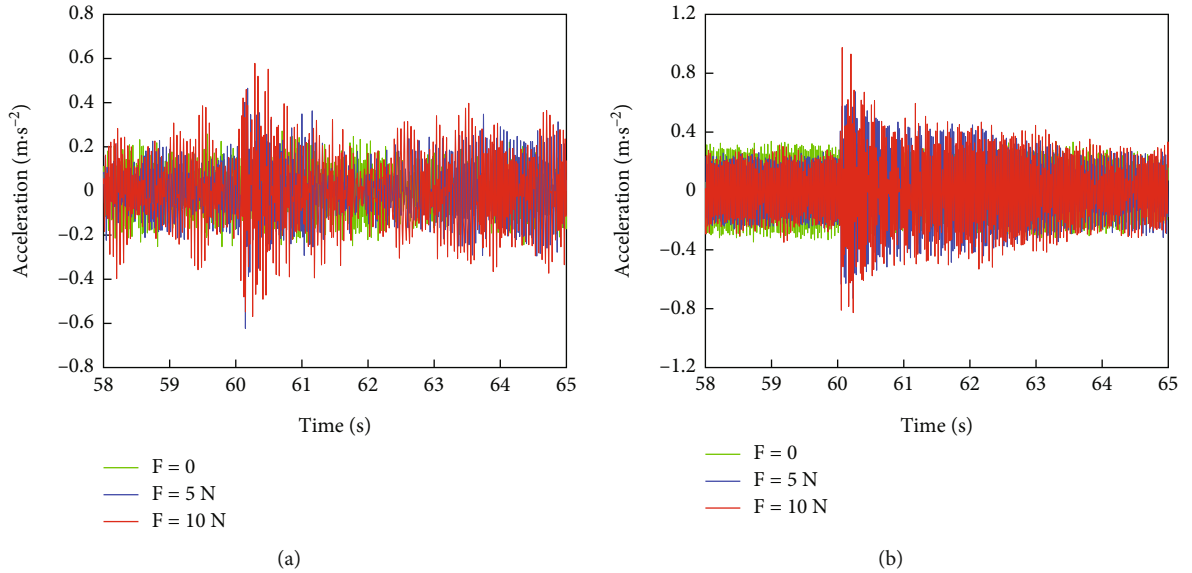FIGURE 13: Acceleration response with LMS-IOBR. (a) 1# point. (b) 2# point.

FIGURE 14: Acceleration response with multichannel LMS at secondary path mutation (58-65 s). (a) 1# point. (b) 2# point.

$|\angle(G_{11}(\omega)) - \angle(\widehat{G}_{11}(\omega))| = 3.58°$ and amplitude error is $||G_{11}(\omega)| - |\widehat{G}_{11}(\omega)||/|G_{11}(\omega)| = 72.5\%$. In contrast, phase error and amplitude error of the constructed equivalent secondary path $Geq_{11}(\omega_1)$ are only 1.21° and 41.0%, which is far less than those of $G_{11}(\omega)$. Furthermore, the same is true for the changing trend of $G_{11}(\omega_2)$ and $G_{11}(\omega_2)$. As a result, the proposed LMS-IOBR shows significant damping compensation effects on the secondary path so as to have stronger adaptability to varying system parameter changes, which is beneficial to improve the robustness and effectiveness of helicopter ACSR during maneuver flight.

5.3. Time-Varying Rotor Load Excitation. In order to reproduce load changes of amplitude, phase, and frequency in

maneuver flight, the excitation amplitude is set as follows at 40 s: $F(t) = [1 + 0.15 \sin (0.2 \times 2\pi t)] \times F_0(t)$, which means that excitation force fluctuates in the form of a sine signal with a frequency of 0.2 Hz, and the fluctuation value is 15% of the initial value. Excitation phase increases 45° at 60 s, and the two excitation frequencies simultaneously decrease 5% at 80 s. Control starts at 20 s. The turntable remained stationary, and the two control algorithm settings were kept unchanged.

The vibration response and control voltage using multichannel LMS and LMS-IOBR are illustrated in Figures 17 and 18, respectively. Compared with multichannel LMS, LMS-IOBR shows faster convergence and better disturbance adaptability after vibration is suppressed. Figures 17(c) and 17(d) demonstrate that with disturbance continuous fluctuation, multichannel LMS gains stability at the expense of
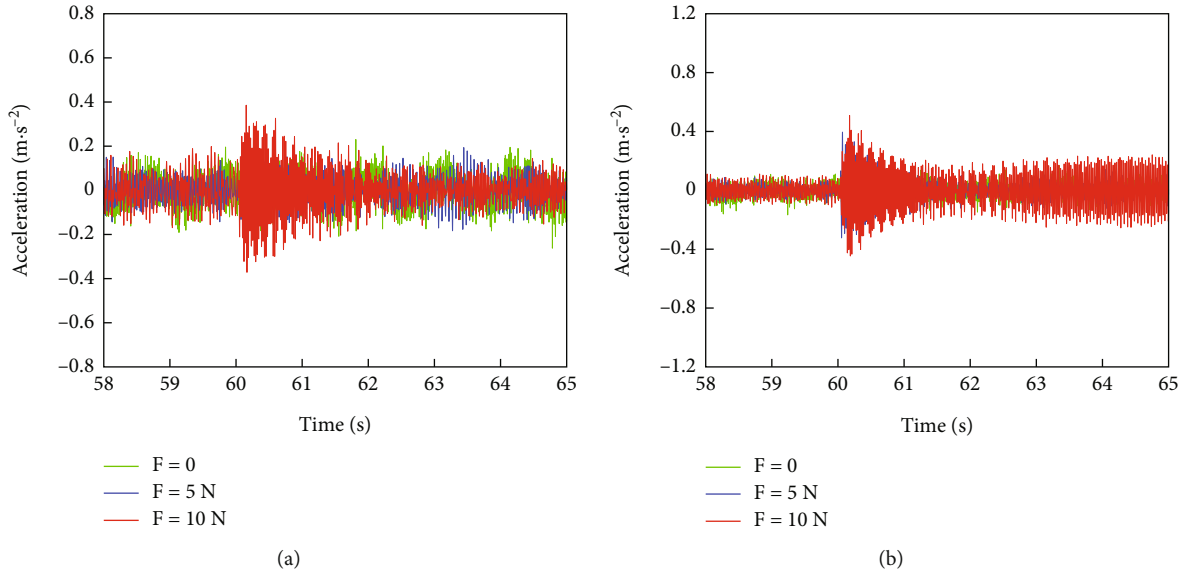
FIGURE 15: Acceleration response with LMS-IOBR at secondary path mutation (58-65 s). (a) 1# point. (b) 2# point.
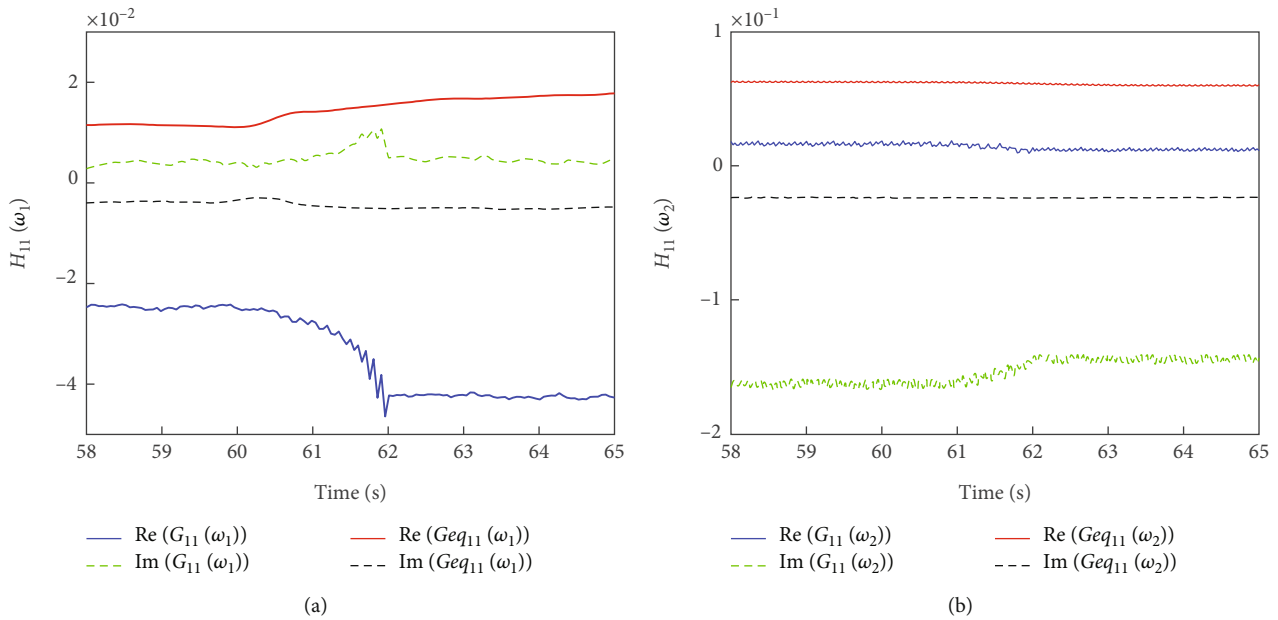

FIGURE 16: Actual secondary path $G_{11}(\omega)$ and equivalent secondary path $Geq_{11}(\omega)$ before and after system parameter mutation (58-65 s). (a) $G_{11}(\omega_1)$ and $Geq_{11}(\omega_1)$. (b) $G_{11}(\omega_2)$ and $Geq_{11}(\omega_2)$.

slow adjustment speed, making the vibration response at the control point increase with excitation changes. In contrast, as is shown in Figures 18(c) and 18(d), the output of control voltage in LMS-IOBR is adjusted quickly, speeding up convergence and ensuring system stability at the same time.

On the other hand, excitation phase mutation causes discontinuous changes of uncontrolled vibration, which widened the phase gap between desired signal and the secondary response contributed by PSAs, leading to the residual vibration increasement. It takes at least 20 s for multichannel LMS to converge, while the proposed LMS-IOBR

adjusts the control signal phase rapidly, and error response is suppressed within 7 s, showing better performance of tracking disturbance and adapting to changes.

5.4. Simulating Continuous Subduction-Uplift Helicopter Maneuver Condition. To fully simulate helicopter ACSR in maneuver flight, continuous changes of harmonic excitation and secondary path need considering simultaneously. First 10 s is the control process after vibration is stabilized, when the turntable remains still. From 10 s on, external disturbance changes every 10 s and frequency decreases 5%. In each change, excitation phase raises 30° and amplitude is

TABLE 5: $G_{11}(\omega)$ and $Geq_{11}(\omega)$ before and after system parameter mutation.

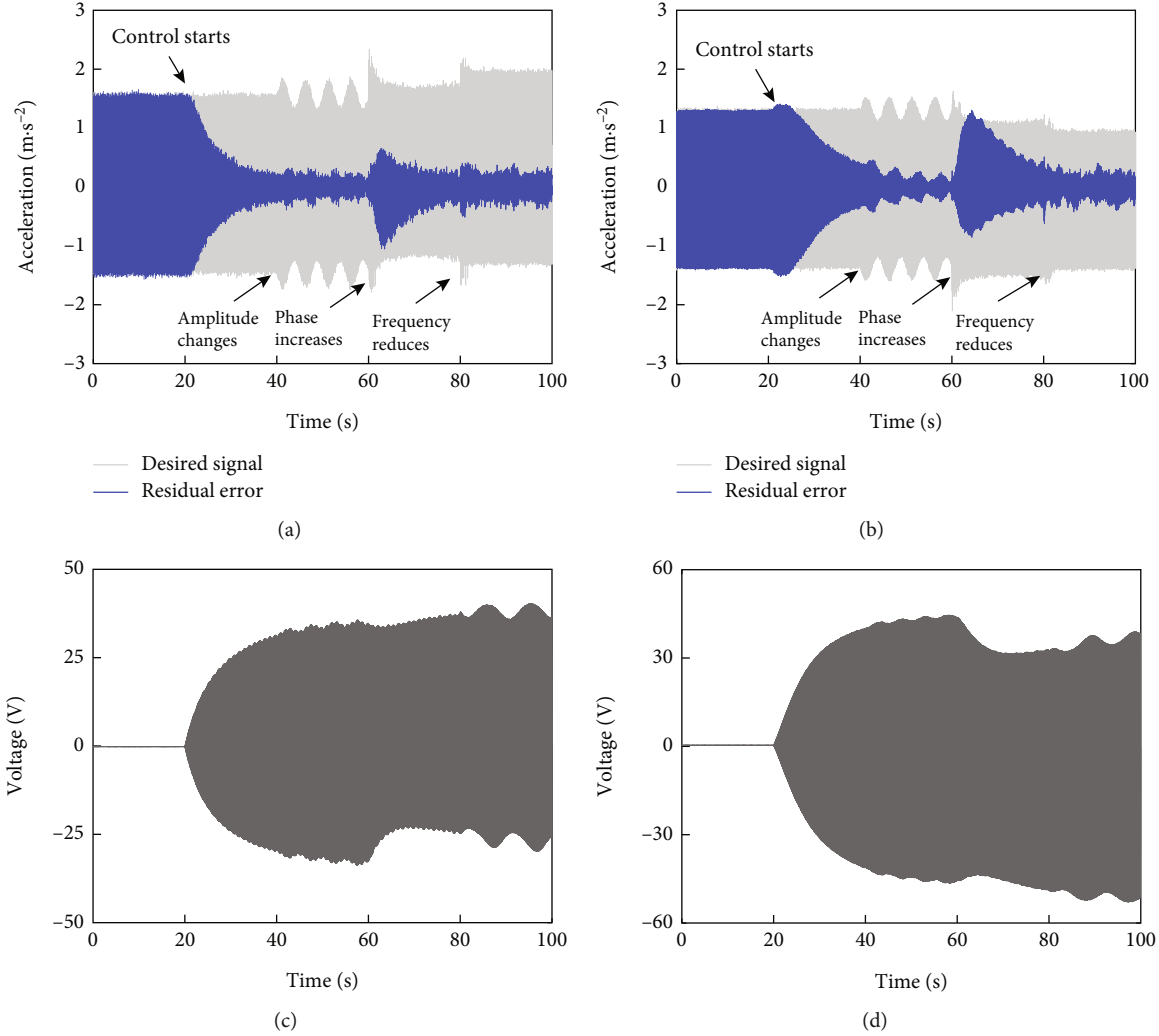|	$H_{11}(\omega)/(\mathrm{m}\cdot\mathrm{s}^{-2}/\mathrm{V})$	$\widehat{H}_{11}(\omega)/(\mathrm{m}\cdot\mathrm{s}^{-2}/\mathrm{V})$	Phase error	Amplitude error
$G_{11}(\omega_1)$	$-2.42\times10^{-2}+0.40\times10^{-2}i$	$-4.21\times10^{-2}+0.43\times10^{-2}i$	$3.58°$	72.5%
$Geq_{11}(\omega_1)$	$1.12\times10^{-2}-0.36\times10^{-2}i$	$1.59\times10^{-2}-0.47\times10^{-2}i$	$1.21°$	41.0%
$G_{11}(\omega_2)$	$1.83\times10^{-2}-1.66\times10^{-1}i$	$1.09\times10^{-2}-1.41\times10^{-1}i$	$1.87°$	15.3%
$Geq_{11}(\omega_2)$	$6.24\times10^{-2}-2.36\times10^{-2}i$	$5.98\times10^{-2}-2.32\times10^{-2}i$	$0.49°$	3.9%

FIGURE 17: Acceleration response and control voltage with multichannel LMS. (a) Acceleration response at 1# point. (b) Acceleration response at 2# point. (c) Control voltage of 1# PSA. (d) Control voltage of 2# PSA.

increased by 50% within 2 s, which remains unchanged until it decreases to initial within the last 2 s. According to reference [14], fuselage pitch angle of UH-60A helicopter changes about 30° during pull-up maneuver in high-speed forward flight. Therefore, the turntable is driven to rotate back and forth between 154° and 186° within 5 s. Figure 19 displays the changing process of the elastic beam position. The turntable stops moving at 40 s, and the amplitude and frequency of excitation return to the original value.

As we can see from Figures 20 and 21, vibration response of the elastic beam has achieved satisfactory attenuation before excitation changes. However, uncontrolled response surges due to the sudden change of disturbance phase and amplitude sharp increasement. Multichannel LMS shows poor adaptability to complex disturbance and secondary path changes. After continuous secondary path changes caused by the elastic beam reciprocating motion, the peak value of the controlled
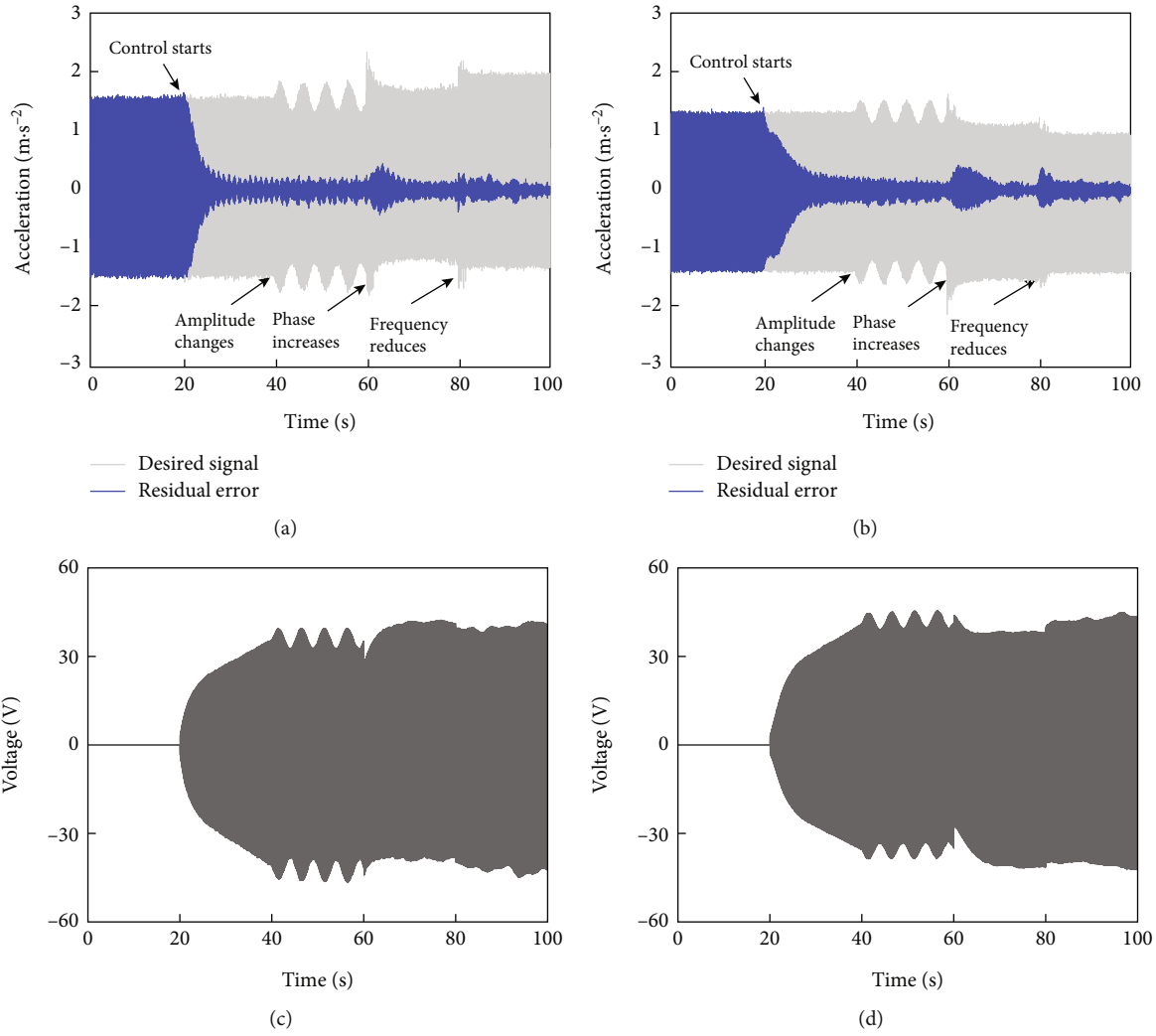
FIGURE 18: Acceleration response and control voltage with LMS-IOBR. (a) Acceleration response at 1# point. (b) Acceleration response at 2# point. (c) Control voltage of 1# PSA. (d) Control voltage of 2# PSA.
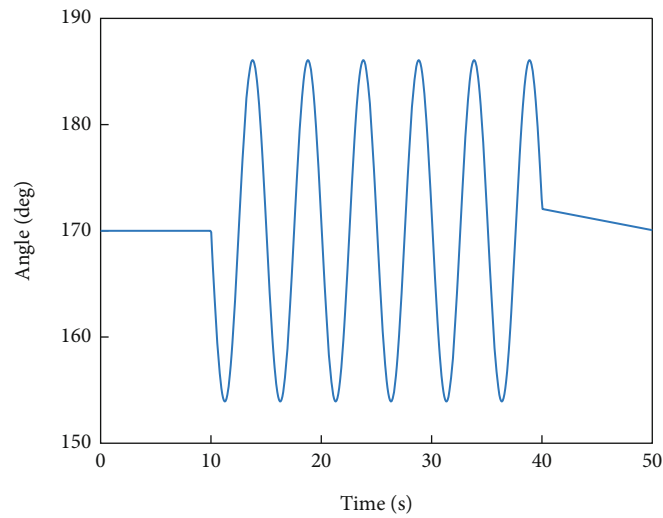

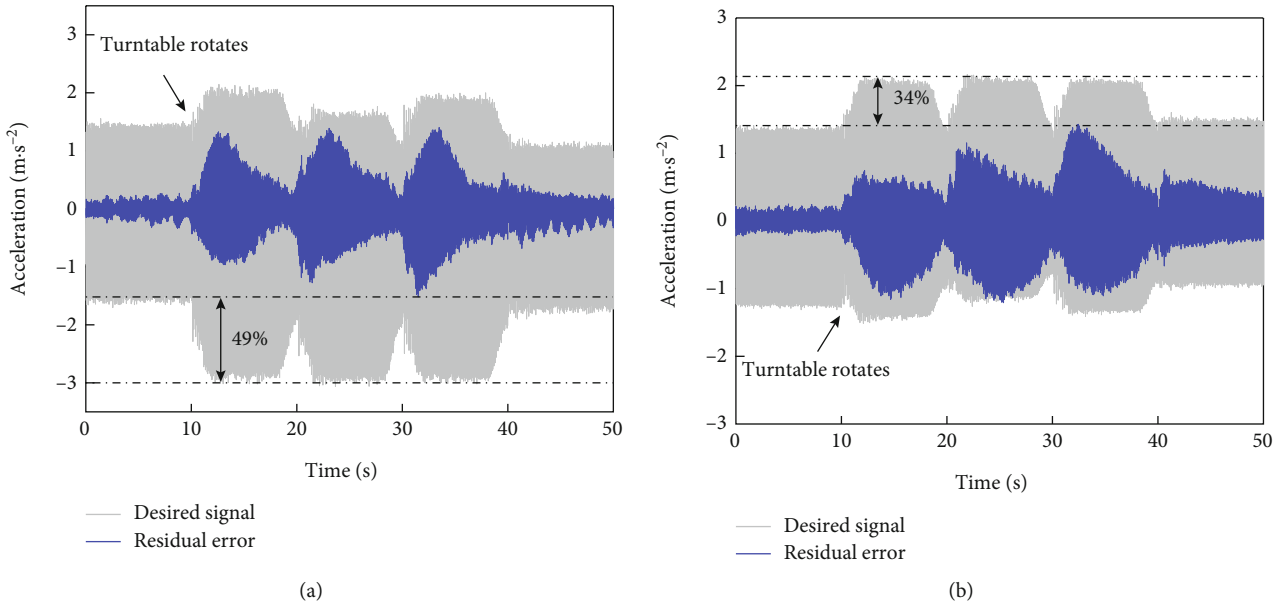FIGURE 19: Changing process of the turntable azimuth angle.

(a)

(b)

FIGURE 20: Acceleration response with multichannel LMS. (a) 1# point. (b) 2# point.
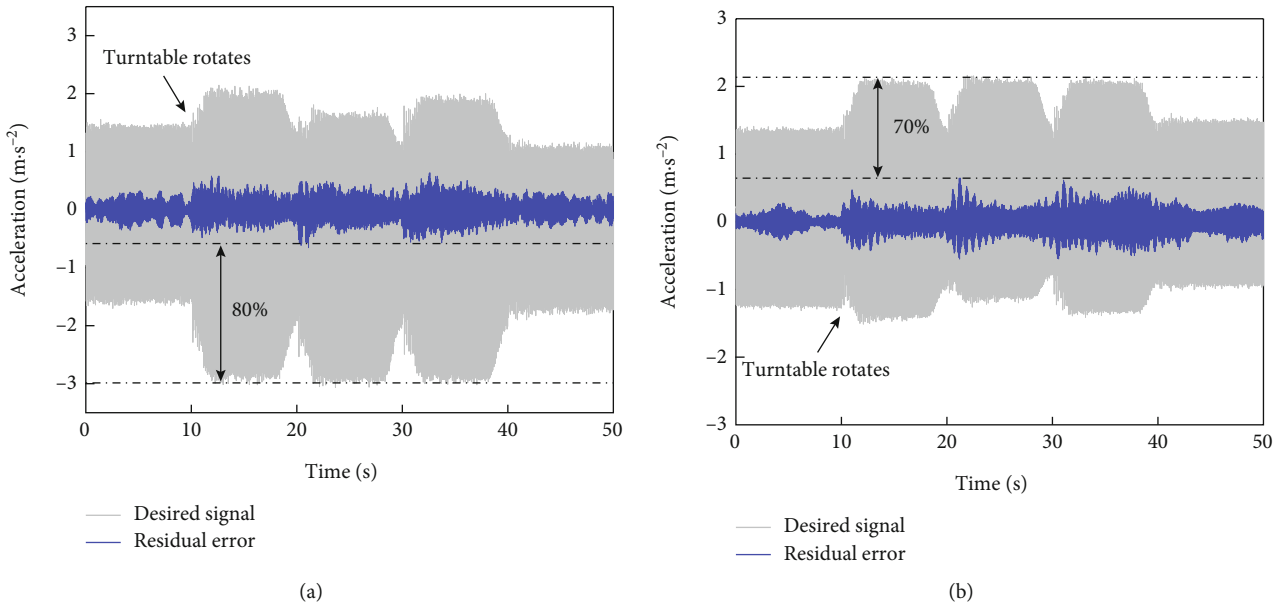

(a)

(b)

FIGURE 21: Acceleration response with LMS-IOBR. (a) 1# point. (b) 2# point.

response at 1# and 2# control points continues to increase, which is only 49% and 34% lower than that of the uncontrolled response. In contrast, LMS-IOBR displays good applicability to simulating continuous subduction-uplift helicopter maneuver condition. Figure 21 shows that the peak response of closed-loop system attenuates 80% and 70%, and the vibration is reduced to 15% and 20%, respectively, within 3 s, which verifies fast convergence and adaptability to the secondary path. Experiment results demonstrate that the proposed LMS-IOBR can suppress harmonic vibration in the time-varying secondary path effectively, showing strong transient adaptability and robustness.

6. Conclusions

To solve the problems of the secondary path mutation and time-varying external excitation during helicopter maneuver flight, an improved LMS-IOBR algorithm is proposed. Vibration control simulations are carried out based on a simplified helicopter finite element model. The ACSR experiments are conducted on a designed elastic beam rotating test platform which can simulate helicopter's continuous subduction uplift. The main conclusions are summarized as follows:

(1) The system model in the target frequency band can be identified through input-output data in the

LMS-IOBR, and the output form of the feedback controller is designed based on the ARMAX model. The simulation results of the secondary channel mutation and the complex time-varying disturbance reveal that real-time computation of LMS-IOBR is reduced by 52%, showing fast convergence and strong robustness while ensuring control effects

(2) In rotating ACSR experiments on the rotating test platform, the LMS-IOBR algorithm shows obvious advantages over multichannel LMS in adaptive regulation performance, robustness, and convergence speed. The experimental results demonstrate that LMS-IOBR can suppress harmonic vibration response under the complex conditions of external disturbance and sudden changes of the secondary channel during helicopter maneuver flight, revealing strong robustness and transient adaptability

In the future, the effectiveness of the proposed controller could be validated through the helicopter maneuver flight experiments.

Data Availability

The data used to support the findings of this study are included within the article.

Conflicts of Interest

The authors declare that they have no conflicts of interest.

Acknowledgments

References

[1] A. Staple and D. Wells, "The development and testing of an active control of structural response system for the EH-101 helicopter," in *Proceedings of the 16th European Rotorcraft Forum*, vol. 9, London, UK, 1990.

[2] R. Goodman and T. Millott, "Design, development and flight test of the active control system for the Sikorsky S-92," in *Proceedings of the American Helicopter Society 56th Annual Forum*, pp. 764–771, San Francisco, USA, 2000.

[3] T. A. Millott, R. K. Goodman, J. K. Wong, W. A. Welsh, J. R. Correia, and C. E. Cassil, "Risk reduction flight test of a preproduction active vibration control system for the UH-60M," in *Annual Forum Proceedings-American Helicopter Society*, vol. 59, pp. 223–230, Phoenix, USA, 2003.

[4] B. Vignal and T. Krysinski, "Development and qualification of active vibration control system for the Eurocopter EC225/EC725," in *Annual Forum Proceedings-American Helicopter Society*, vol. 61, pp. 96–106, Grapevine, USA, 2005.

[5] J. C. Walchko, J. S. Kim, and K. W. Wang, "Hybrid feedforward-feedback control for active helicopter vibration suppression," in *63rd American Helicopter Society International Annual Forum*, vol. 2, pp. 1260–1276, United States, 2007.

[6] X. Ma, Y. Lu, and F. Wang, "Experimental investigations on active control of multi-frequency helicopter vibrations using discrete model predictive sliding mode control," *Proceedings of the Institution of Mechanical Engineers, Part G: Journal of Aerospace Engineering*, vol. 232, no. 15, pp. 2898–2909, 2018.

[7] L. Pan and R. Chen, "Formulation and validation of a helicopter model for pull-up maneuver simulation," *Acta Aeronautica et Astronautica Sinica*, vol. 31, no. 12, pp. 2315–2323, 2010.

[8] M. Bhagwat, R. Ormiston, H. Saberi, and H. Xin, "Application of CFD CSD coupling for analysis of rotorcraft airloads and blade loads in maneuvering flight," in *Proceedings of the American Helicopter Society 63rd Annual Forum*, Virginia Beach, USA, 2007.

[9] U. Arnold and D. Fuerst, "Closed loop IBC results from CH-53G flight tests," *Aerospace Science and Technology*, vol. 9, no. 5, pp. 421–435, 2005.

[10] E. M. Huff, I. Y. Tumer, E. Barszcz, M. Dzwonczyk, and J. McNames, "An Analysis of maneuvering effects on transmission vibrations in an AH-1 Cobra helicopter," *Journal of the American Helicopter Society*, vol. 47, no. 1, pp. 42–49, 2002.

[11] A. V. Popov, "Proof-of-match technique for Bell 427 helicopter level D simulator, [Ph.D. thesis]," Montreal, School of Superior Technology, 2005.

[12] F. Hoffmann, R. Maier, P. Jänker, F. Hermle, and A. Berthe, "Helicopter interior noise reduction by using active gearbox struts," in *12th AIAA/CEAS Aeroacoustics Conference (27th AIAA Aeroacoustics Conference)*, Cambridge, Massachusetts, 2006.

[13] Y. Lu, Z. Gu, A. Lin, and M. Li, "Flight test of active control of structure response for helicopter," *Journal of Vibration Engineering*, vol. 25, no. 1, pp. 24–29, 2012.

[14] D. Meng, P. Xia, and L. S. Song, "MIMOMH feed-forward adaptive vibration control of helicopter fuselage by using piezoelectric stack actuators," *Journal of Vibration and Control*, vol. 24, no. 23, pp. 5534–5545, 2018.

[15] Y. Lu and J. Feng, "A time-domain active vibration control algorithm for helicopter based on a prior error channel identification strategy," *Shock and Vibration*, vol. 2018, Article ID 2870896, 11 pages, 2018.

[16] S. Kuo and D. Morgan, *Active Noise Control Systems–Algorithms and DSP Implementations*, John Wiley & Sons Inc, 1996.

[17] X. Shao, H. Si, and W. Zhang, "Event-triggered neural intelligent control for uncertain nonlinear systems with specified-time guaranteed behaviors," *Neural Computing and Applications*, vol. 33, no. 11, pp. 5771–5791, 2021.

[18] X. Shao, H. Si, and W. Zhang, "Low-frequency learning quantized control for MEMS gyroscopes accounting for full-state constraints," *Engineering Applications of Artificial Intelligence*, vol. 115, article 104724, 2022.

[19] H. Wang, X. Shao, J. Li, and J. Liu, "A velocity-free adaptive RISE-based trajectory tracking approach for quadrotors with desired model compensation," *Aerospace Science and Technology*, vol. 92, pp. 551–562, 2019.

[20] X. Shao, L. Xu, and W. Zhang, "Quantized control capable of appointed-time performances for quadrotor attitude tracking: experimental validation," *IEEE Transactions on Industrial Electronics*, vol. 69, no. 5, pp. 5100–5110, 2022.

[21] S. Li, X. Shao, W. Zhang, and Q. Zhang, "Distributed multicircular circumnavigation control for UAVs with desired angular spacing," *Defence Technology*, 2023.

[22] X. Shao, S. Li, J. Zhang, F. Zhang, W. Zhang, and Q. Zhang, "GPS-free collaborative elliptical circumnavigation control for multiple non-holonomic vehicles," *IEEE Transactions on Intelligent Vehicles*, pp. 1–12, 2023.

[23] Y. Yang, X. Shao, Y. Shi, and W. Zhang, "Back-stepping robust control for flexible air-breathing hypersonic vehicle via α-filter-based uncertainty and disturbance estimator," *International Journal of Control, Automation and Systems*, vol. 19, no. 2, pp. 753–766, 2021.

[24] X. Shao, S. Li, W. Zhang, and E. Q. Wu, "Distance-based elliptical circumnavigation control for non-holonomic robots with event-triggered unknown system dynamics estimators," *IEEE Transactions on Intelligent Transportation Systems*, pp. 1–13, 2023.

[25] Y. F. Qin, Y. Lu, J. C. Ma, and H. Y. Yue, "Active vibration control of helicopter maneuvering flight using feedforward-robust hybrid control based on reference signal reconstruction," *Shock and Vibration*, vol. 2021, Article ID 3153531, 17 pages, 2021.

[26] D. Heverly, K. W. Wang, and E. C. Smith, "Optimal actuator placement and active structure design for control of helicopter airframe vibrations, [Ph.D. thesis]," The Pennsylvania State University, 2002.

[27] I. D. Landau, T. B. Airimitoaie, A. Castellanos-Silva, and A. Constantinescu, *Adaptive and Robust Active Vibration Control Methodology and Tests*, Springer International Publishing Press, 2017.

[28] R. M. Howard, *Linear System Theory*, Wiley-IEEE Press, 2002.

[29] X. G. Zhang, *Helicopter Design for Dynamics*, Aviation industry Press, 1995.

[30] C. F. Zhao, "Study on active control of structural responses for helicopter in frequency domain, [M.S. thesis]," Nanjing University of Aeronautics and Astronautics, 2010.